

Article

Study on Denoising Method of Photoionization Detector Based on Wavelet Packet Transform

Zengyuan Liu ^{1,2}, Xiujuan Feng ^{1,2,*}, Chengliang Dong ¹ and Mingzhi Jiao ³¹ School of Mines, China University of Mining and Technology, Xuzhou 221116, China² Rare Earth Research Institute, China University of Mining and Technology, Xuzhou 221116, China³ National and Local Joint Engineering Laboratory of Internet Application Technology on Mine, China University of Mining and Technology, Xuzhou 221116, China

* Correspondence: xjfeng@cumt.edu.cn

Abstract: Aiming at the task of noise suppression caused by the photoionization detector (PID) monitoring signal of volatile organic compounds (VOCs) due to local non-uniformity of the photo-cathode surface of PID in the ionization chamber, this paper proposes an analytical method of a PID signal with the adaptive weight of the small wave package decomposition node. The PID signal is transmitted to the upper machine software through the single-chip microcontroller. The appropriate wavelet packet decomposition level is determined according to the time frequency characteristics of the original signal of the PID, and the optimal wavelet packet base is selected through the polynomial fitting of the signal quality evaluation index. By comparing the quality of signals processed by the traditional wavelet packet denoising method and the denoising method presented in this paper, the superiority of the proposed method in the denoising signals of PID was verified. This method can eliminate the noise generated by local non-uniformity on the photocathode surface of the PID ionization chamber in a high humidity environment, which lays a foundation for the accurate monitoring of VOCs in a high humidity environment.

Keywords: wavelet packet transform; evaluation of quality; optimal wavelet packet base; signal denoising; VOCs



Citation: Liu, Z.; Feng, X.; Dong, C.; Jiao, M. Study on Denoising Method of Photoionization Detector Based on Wavelet Packet Transform.

Chemosensors **2023**, *11*, 146.
<https://doi.org/10.3390/chemosensors11020146>

Academic Editors: Fanli Meng, Zhenyu Yuan and Dan Meng

Received: 25 December 2022

Revised: 12 February 2023

Accepted: 13 February 2023

Published: 16 February 2023



Copyright: © 2023 by the authors. Licensee MDPI, Basel, Switzerland. This article is an open access article distributed under the terms and conditions of the Creative Commons Attribution (CC BY) license (<https://creativecommons.org/licenses/by/4.0/>).

1. Introduction

Volatile organic compounds (VOCs) usually refer to organic compounds with a boiling point between 50 °C and 260 °C under normal pressure [1]. VOCs affect the environmental quality and are carcinogenic and mutagenic to the human body [2–4]. At present, the monitoring of VOCs mainly includes photoionization detection (PID), Fourier transform infrared spectrometry (FTIR), and gas chromatography-mass spectrometry (GC-MS), flame ionization detection (FID), metal oxide semiconductor sensors (MOS), differential optical absorption spectroscopy (DOAS), and other methods. The maintenance cost of FTIR optical equipment is high and it requires a large maintenance amount. The detection cycle of the GC-MS samples is relatively long. In addition, different detectors have different amounts of sensitivity, selectivity, accuracy, and equipment maintenance. When FID monitors VOCs, oxygen, moisture, and organics containing nitrogen, oxygen, or halogen atoms in the flue gas can interfere with the test; VOCs detected by DOAS are of limited variety. At present, it can mainly monitor benzene, toluene, and other benzene series [5]. Currently, portable VOC monitoring methods are widely used including PID and MOS. Fanli Meng et al. [6–9] used Au/SnO₂/RGO nanocomposites to prepare MOS sensors, which can monitor 1–1000 ppm of ethanol. MOS sensors made of reduced GO/carbon monoxide nanocomposites can monitor 1 ppb of xylene. The response time of the sensor was shortened by LaCoO₃ modified ZnO, and the optimum temperature of four alcohol homologous gases monitored by a ZnO sensor was studied. However, MOS gas sensors have poor selectivity.

PID is one of the most widely used portable VOC gas detection technologies. The measurement accuracy of the PID is used through the proper denoising method, which has always been employed by scholars both domestic and abroad. Rezende [10] used the digital moving average filtering method to decrease the noise of the PID sensor data to obtain a lower limit of toluene monitoring. Agbroko et al. [11] used first-order low-pass filtering to reduce the noise of the PID sensor, and obtained a sensor signal with a high signal-to-noise ratio for the analysis of the total content of VOCs and the content of each component. Je C et al. reported that in a multi-channel VOC monitoring system, the average value filtering was used to lower the noise of the PID sensing data, and the optimal average value sampling number was found through experiments. Liu Chang [12] compared the advantages and disadvantages of VOC monitoring based on PID. The effects of the limited filtering method, median filtering method, arithmetic average filtering method, recursive average filtering method, median average filtering method, the median value average filtering method, and the median average filtering method have been discussed in detail. Finally, the median average filtering method is applied for the optimal sensor data, and the data of the VOC monitoring sensor with a high signal-to-noise ratio can be obtained. At present, the noise of the PID signal is mostly filtered by median filtering and the low-pass filtering method [13]. The two filtering means separate the useful signal and the noise signal in the time domain by Fourier transform in the frequency domain, but the separation can be completed only when the useful signal and the noise signal are not mixed together, and the noise of the signal is often distributed in the whole frequency domain, so when removing the noise, the useful signal is often removed. Considering that the noise of the signal is often distributed in the entire frequency domain, useful signals are often removed simultaneously while removing noise [14–17]. Therefore, at present, the method of the denoising of PID sensors used for VOC monitoring at home and abroad takes effect at the cost of sacrificing signals. The wavelet analysis method can analyze the time frequency of the signal, overcoming the shortcomings of traditional filtering method that works only for frequency domain analysis [18–20]. Based on the analysis of traditional wavelet packet transform, this article proposes a method of decomposing the energy-adaptable weight of the small wave bag decomposition node. This method overcomes the problem of the traditional wavelets when removing the noise of the signal. Therefore, the accuracy of the VOC quantitative analysis is improved. This article verifies the superiority of the method of removing noise in small traditional wavelets through the signal quality evaluation results.

2. VOC Monitoring Device

The composition of the VOC monitoring device is as follows (Figure 1): single-chip module, PID module, A/D conversion module, serial port transmission module, and upper machine module. The PID enables VOCs to generate a current under high UV lamps. The current in the PID will generate a voltage value through a fixed resistor. After the analog voltage is converted by an A/D converter, it is displayed on a single-chip micro tube in a digital voltage form. The single-chip control serial port to send the data to the upper machine software was developed by C#. The time domain waveform generated by the sensor can be displayed and stored in the computer. The frequency domain signal stored by the upper machine software can be imported into MATLAB to perform denoising work on the light ionized sensor signal.

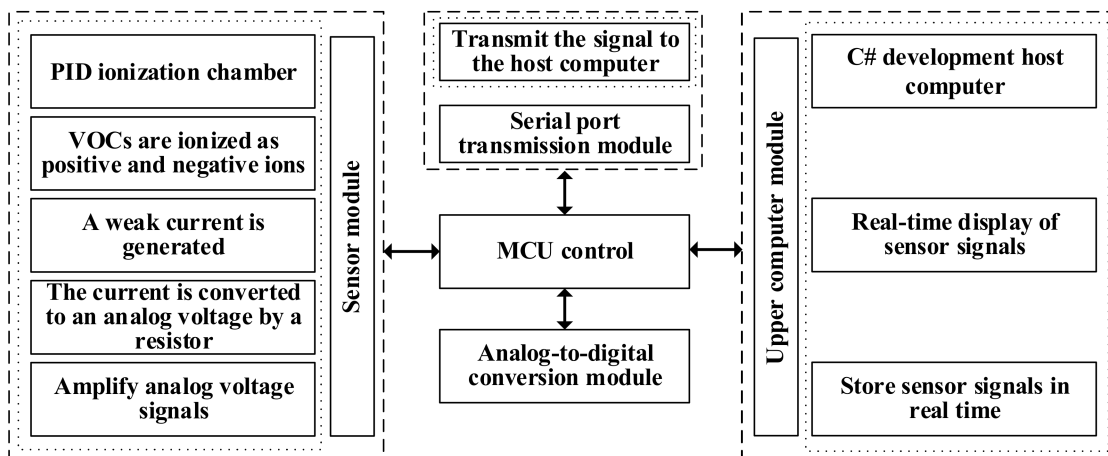


Figure 1. Composition of the VOC monitoring device.

2.1. PID Module

Photoionization detection (PID) is the simplest technology to detect VOCs [21–23]. Its working principle (Figure 2) [24–26] is that a UV lamp acts as the light source, and the detected gas is passed into the ionization chamber, which is irradiated by UV light and decomposed into detected signals—electrons and ions. Under the action of an electric field, electrons and ions move to the positive and negative electrodes, respectively, to form the current, and the current is output after amplification. After the resistance of the fixed resistance value, the voltage value is output to realize the quantitative test of its gas concentration. The principle of a photoionization detector is shown in Figure 2.

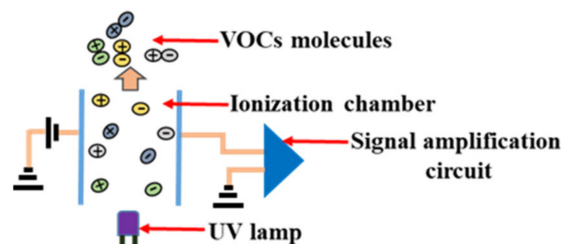


Figure 2. Working principle diagram of the PID of VOCs.

In this device, a Shenyang Magnesium Technology Light ion gas sensor is used for VOC monitoring. The sensor has an ultra-small UV lamp of 10.6 eV (i.e., manufacturer: Shenyang Magnesium Technology, type: krypton gas lamp, window: magnesium fluoride, power: 0.5 W) that can monitor VOCs such as benzene, ketones, and aldehydes with an ionization potential of less than 10.6 eV. When the VOC concentration is 0, the PID voltage value is 0.043 V, the response time of PID is less than 3 s, and a VOC gas of 200 ppb–2000 ppm can be detected [27]. It also has different response values for different VOCs. The working temperature range is −20–60 °C. The sensor has three pins, which are power supply voltage pins, ground pins, and signal transmission pins, respectively. The XPT2046 modulus conversion chip is controlled by the single chip microcomputer in the signal transmission pins.

2.2. Single-Machine Serial Port Transmission Module

In the VOC monitoring device, the data acquisition and control unit of the light ionized sensor uses a STC89C52RC single-chip microcomputer to complete the content of the unit [28,29]. The STC89C52RC single-chip microcomputer is an 8-bit micro-controller developed by Hongjing Company, Wuhu, China, with an operating frequency of 12 MHz, a built-in 512 B memory and an 8 kB storage space. This device uses Keil Uvision 5 to record the C language into the single-chip machine.

The STC89C52 single-chip microcomputer does not have an A/D conversion function, so the module conversion module uses the XPT2046 chip controlled by a single-chip microcomputer. The XPT2046 contains a 12-bit resolution 125 kHz conversion rate to approach the A/D converter one by one to meet the real-time monitoring of the PID sensor to monitor VOCs. The PID signal output pins are connected to the AIN3 pin of the single-chip microcomputer with the DuPont line, and the PID and XPT2046 chip are together.

The serial port is a very widely used communication interface as it is cheap, easy to use, and the communication lines are simple, which can realize the interoperability of the single-chip microcomputer and the upper machine. The STC89C52RC single-chip microcontroller comes with UART (Universal Asynchronous Receiver Transmitter). The sensor data are passed to the upper machine by the serial port.

2.3. Design of the Upper Machine Module

The development of the upper-bit machine in the serial communication system used by a single-chip microcomputer for volatile organic matter monitoring was implemented in the development environment of Visual Studio 2015 [30]. The main function of the upper machine is to receive the signal value of the PID sensor through the microcontroller serial port and draw the waveform of the signal to generate the signal. First, we added serial ports, then added the GROUPBOX control to the window design, next, we added ComboBox1 to the selection of the port slogan in the GROUPBOX control range, added Combobox2 for the choice of baud rate, and then we finally added two radio button controls to select the receiving serial port transmission data. The pattern, the number, and character mode were chosen, three button controls were added to control the open port, closed port, and waveform display, then textbox control was added to display the signal value of the sensor.

2.4. VOCs Online Detection Device and Method

Since the response value of PID is easily affected by environmental factors such as temperature and humidity, the experimental device (Figure 3) was built in a fume hood room with stable environmental conditions. The indoor temperature of the ventilation cabinet was 25 degrees Celsius and the air pressure was 1.01×10^5 Pa. The standard gas used in this article was derived from Jining Xieli Specialty Co. Ltd., Jining, China. A standard gas bottle capacity is 8 L, the concentration of the standard gas is 2000 ppm benzene gas, and the gas is filled with nitrogen. A quality flowmeter was used to control the amount of the standard gas to calculate the content of the standard gas. The unit of the quality flowmeter is in L/min. Through Equation (1), the concentration of the standard gas can be calculated and its unit can be converted to mg/L to facilitate the calculation of the gas content in the gas cylinder. Among them, C is the mass concentration (mg/m^3) of benzene gas, X is the volume concentration 2000 ppm, and M is the molar mass of benzene.

$$X = C \times 24.5/M \quad (1)$$

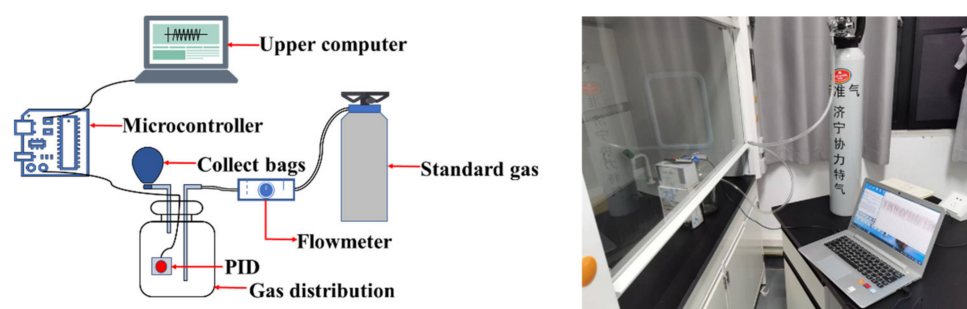


Figure 3. Experimental device of the PID module denoising for the online detection of VOCs.

The gas from the standard gas cylinder is introduced into the collecting cylinder with a capacity of 3 L. A certain concentration of benzene gas can be prepared in the collecting cylinder by controlling the flow rate and time of gas in the standard cylinder. The VOC monitoring module is shown in Figure 3.

The standard gas flow rate was 0.05 L/min, and the time was 10 s. The phenyl gas concentration in the gas cylinder was 5.57 ppm. The noise-containing PID response signal under this concentration is shown in Figure 4.

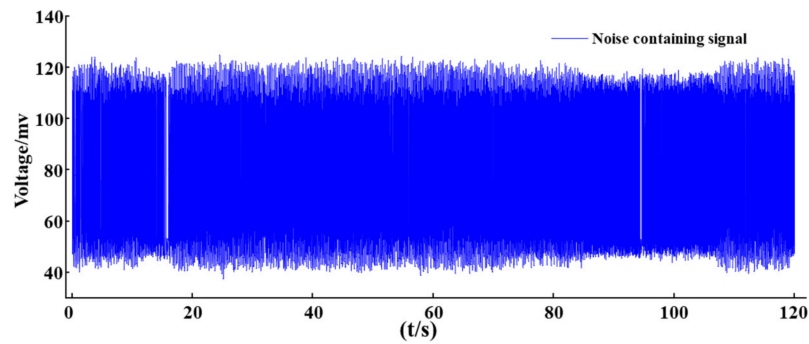


Figure 4. PID original signal.

3. PID Sensor Signal Denoising Method Based on Wavelet Analysis

3.1. Selection of a Wavelet Decomposition Level

Given the orthogonal scale function $\varphi(x)$ and its corresponding small wave function $\psi(x)$, there is [31–34]:

$$\begin{cases} \varphi(x) = \sqrt{2} \sum_{k \in \mathbb{Z}} q_k \varphi(2x - k) \\ \psi(x) = \sqrt{2} \sum_{k \in \mathbb{Z}} g_k \varphi(2x - k) \end{cases} \quad (2)$$

where q_k and g_k are the conjugation filters; q_k is the low-pass filter coefficient; g_k is the high-pass filter coefficient.

Set $\mu_0 = \varphi(x)$, $\mu_1 = \psi(x)$, at this time:

$$\begin{cases} \mu_{2n}(x) = \sqrt{2} \sum_{k \in \mathbb{Z}} q_k \mu_n(2x - k) \\ \mu_{2n+1}(x) = \sqrt{2} \sum_{k \in \mathbb{Z}} g_k \mu_n(2x - k) \end{cases} \quad (3)$$

Among them, n is the n -wave sequence when the decomposition scale is j .

Define V_j^n as a closure space for the function $\mu_n(x)$, V_j^{2n} is the closure space of $\mu_{2n}(x)$, V_j^{2n+1} is the closure space of $\mu_{2n+1}(x)$, then V_j^n can be decomposed as:

$$V_j^n = V_j^{2n} + V_j^{2n+1} \quad (4)$$

where V_j^{2n} and V_j^{2n+1} meet the conditions of $V_j^{2n} \perp V_j^{2n+1}$.

If the small wave packet coefficients of the signal on V_j^{2n} and V_j^{2n+1} are p_j^{2n} and p_j^{2n+1} , respectively, then the small wave bag decomposition can be obtained by $\{p_k^{j+1,2n}\}$ and $\{p_k^{j+1,2n+1}\}$, which is expressed as [35]:

$$\begin{cases} p_k^{j+1,2n} = \sum_l h_{2l-k} p_l^{j,n} \\ p_k^{j+1,2n+1} = \sum_l g_{2l-k} p_l^{j,n} \end{cases} \quad (5)$$

Among them, $p_k^{j,n}$ indicates that the decomposition coefficient of the k wavebase on the n fork tree with a decomposition scale is j and $p_k^{j+1,2n}$ and $p_k^{j+1,2n+1}$ are $p_k^{j,n}$ of two bit [36].

When the PID signal is ready, the decomposition level of the wavelet packet is first determined, where the decomposition level is too low. The noise and useful information of the signal cannot be effectively separated, and the signal noise cannot be effectively removed. In contrast, if the selected decomposition level is too high, a large amount of useful information of the signal will also be removed to cause the new distortion while removing the noise. Therefore, choosing the appropriate wavelet breakdown level is an important step for sensors to generate the signal noise. This article conducted a 4-layer small wave package decomposition experiment on the signal generated by the light ionization sensor. The number of decomposition layers is shown in Figure 5.

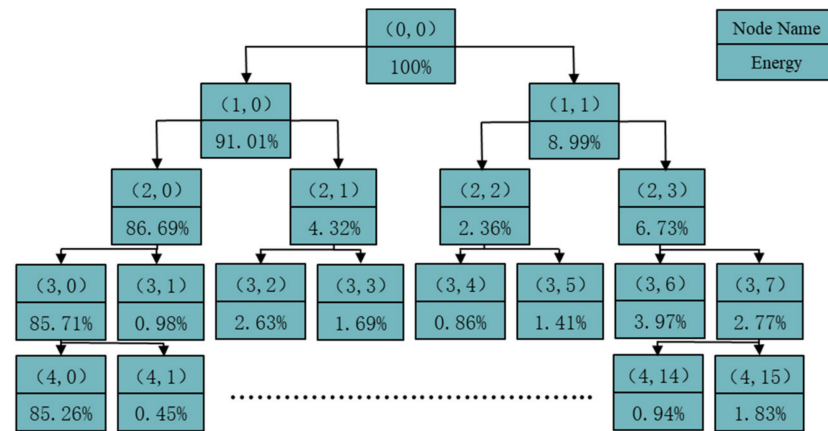


Figure 5. Wavelet packet decomposition node and energy diagram.

According to the Parseval theorem, the total energy of a signal in its time domain is equal to the total energy in the frequency domain. For small waves, just separate the signals and low-frequency components and changes in the form of signals, but the total energy before and after decomposition always remains equal. If a signal $X(T)$ is decomposed to the lower layer, the energy of each sub-band signal can be calculated according to Equation (6) [37–39].

$$E_{ij} = \int |S_{i,j}(t)|^2 dt = \sum_{k=1}^n |x_{i,j}(k)|^2 \tag{6}$$

The distribution of the corresponding energy distribution corresponding to the decomposition trees and decomposition of each node is shown in Figure 5.

The signal-to-noise ratio (SNR) and mean-square error (MSE) of the signal of different wavelets were calculated to decompose the levels to determine the best wavelet breakdown level. SNR represents the ratio of the effective signal energy to noise signal energy. The larger the value of the SNR, the lower the noise effect. The calculation method of the SNR is as shown in Equation (7). MSE represents the degree of similarity between the original signal and the signal after noise. The MSE calculation formula is shown in Equation (8). In this paper, SNR and MSE were used to evaluate the PID signal quality.

$$SNR = 10\lg(s/n) \tag{7}$$

$$MSE = \frac{1}{n} \sum_{i=1}^n (Y_i - \hat{Y}_i)^2 \tag{8}$$

where s and n in SNR represents the effective power of signals and noise, respectively; Y_i in MSE is the original signal; \hat{Y}_i is the signal after noise.

The values of the MSE and SNR of the PID signal after two, three, and four layers of the signal are shown in Table 1.

Table 1. The MSE and SNR of different decomposition levels under the signal.

Evaluation Indicator	2-Layer Decomposition	3-Layer Decomposition	4-Layer Decomposition
SNR	33.0418	36.6291	6.0453
MSE	3.1490	1.3867	6.3679

As shown in Table 1, when the wavelet packet decomposition level was three layers, the SNR value of PID signal was the largest, the MSE was the smallest, and the PID signal processing effect was the best. Therefore, this paper carried out the 3-layer wavelet packet decomposition of the PID signal.

The PID signal collected by the upper machine was decomposed by a three-layer wavelet, the signal was divided into eight frequency bands from low frequency to high frequency, as shown in Figure 6.

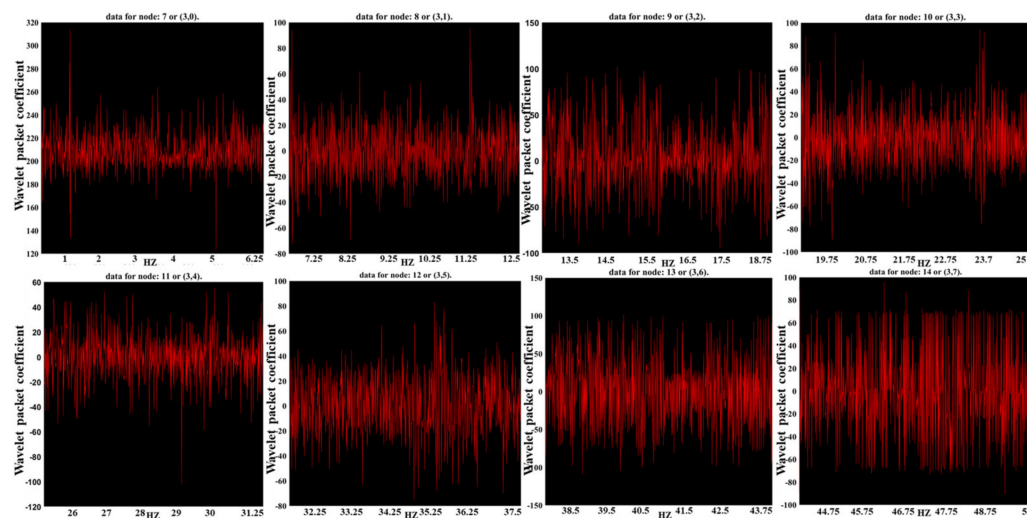


Figure 6. Bior1.3 wavelet packet 3-layer decomposition of 5.57 ppm benzene gas PID with the noise signal.

3.2. Selection of the Wavelet Packet Base

When the wavelet packet changes the PID signal noise, whether the selection of the wavelet base is appropriate will have an important impact on the signal quality after the PID signal processing. After determining the decomposition of the small wave bag as three layers of decomposition, this work used different wavelet packets to perform the experimental analysis of the PID signal denoising, and determined the optimal wavelet packet base based on the results of the signal quality evaluation. The Daubechies (db) wavelet packet base and Symlets (sym) wavelet packet base have an N-order. The Daubechies wavelet packet has good regularity, that is, the smooth error introduced by the wavelet packet as a sparse basis is not easy to detect, which makes the signal reconstruction process smooth. The characteristics of the db wavelet packet are that with the increase in order (sequence N), the larger the order of vanishing moment, the higher the vanishing moment, the better the smoothness, the stronger the localization ability of the frequency domain, the better the division effect of the frequency band, but it will weaken the time domain tight support, and the calculation amount is greatly increased, and the real-time becomes worse. sym is an improvement in the db function. The sym wavelet has better symmetry, which can reduce the phase distortion of signal analysis and reconstruction to a certain extent. The wavelet packet base SNR and MSE of different levels of db and sym were calculated.

By calculating the quality of the 12-order wavelet packet processing signal, the db and sym wavelet packet base were treated with PID. The best order of the PID signal and the optimal wavelet were obtained. The values of the MSE and SNR of the wavelet packet base between db and sym are shown in Table 2.

Table 2. The MSE and SNR of the db and sym wavelet packet base at different levels.

Wavelet Packet Base	MSE	SNR	Wavelet Packet Base	MSE	SNR
db2	1.3541	36.7320	sym2	1.3541	36.7320
db3	1.3213	36.8389	sym3	1.3213	36.8389
db4	1.3892	36.6203	sym4	1.3995	36.5880
db5	1.3719	36.6747	sym5	1.4136	36.5441
db6	1.3722	36.6734	sym6	1.3415	36.7721
db7	1.4312	36.4900	sym7	1.3853	36.6322
db8	1.4004	36.5848	sym8	1.4062	36.5668
db9	1.3803	36.6479	sym9	1.4184	36.5291
db10	1.3886	36.6219	sym10	1.4133	36.5446
db11	1.4221	36.5177	sym11	1.3713	36.6761
db12	1.3832	36.6383	sym12	1.4075	36.5627
db13	1.4323	36.4864	sym13	1.4272	36.5022

Fourier curve fitting was performed on the values of MSE corresponding to the wavelet packet bases of different orders of db, and the Fourier fitting formula is shown as follows.

$$f(a) = a_0 + a_1 \cos(aw) + b_1 \sin(aw) + a_2 \cos(2aw) + b_2 \sin(2aw) + a_3 \cos(3aw) + b_3 \sin(3aw) + a_4 \cos(4aw) + b_4 \sin(4aw) + a_5 \cos(5aw) + b_5 \sin(5aw) \tag{9}$$

The formula's corresponding parameters are shown in Table 3.

Table 3. The db series wavelet packet base corresponded to the parameter value of the MSE fitting function.

$a_0 = 1.4$	$a_1 = 0.0148$	$b_1 = -0.02251$	$a_2 = 0.02968$
$b_2 = -0.02415$	$a_3 = 0.02019$	$b_3 = -0.01056$	$a_4 = 0.03571$
$b_4 = -0.01956$	$a_5 = 0.01173$	$b_5 = -0.0007733$	$w = 0.471$

The corresponding fitting curve is shown in Figure 7.

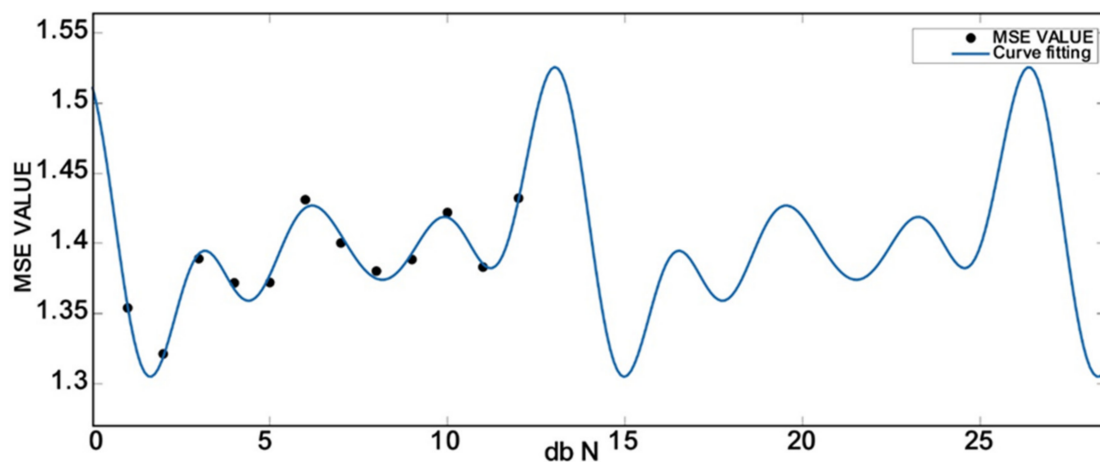


Figure 7. The MSE fitting curve of the db wavelet packet base.

This article evaluated the accuracy of the fitting curve by calculating its decision coefficient. The calculation method is shown in Equation (10).

$$R^2 = 1 - \frac{SS_{res}}{SS_{tot}} = 1 - \frac{\sum(y_i - \hat{y}_i)^2}{\sum(y_i - \bar{y})^2} \tag{10}$$

The R^2 of this polynomial fitting was 0.9826 degrees to meet the minimal value requirements of the MSE of the db wavelet packet base. The minimal value of the MSE of the db wavelet packet base $f(a)_{min}$ was 1.3213

Fourier curve fitting was performed on the SNR values corresponding to the wavelet packet bases of different orders of db, and the Fourier fitting formula was obtained as follows.

$$f(b) = a_0 + a_1 \cos(bw) + b_1 \sin(bw) + a_2 \cos(2bw) + b_2 \sin(2bw) + a_3 \cos(3bw) + b_3 \sin(3bw) + a_4 \cos(4bw) + b_4 \sin(4bw) + a_5 \cos(5bw) + b_5 \sin(5bw) \tag{11}$$

The formula's corresponding parameters are shown in Table 4.

Table 4. The db series wavelet packet base corresponded to the parameter values of the SNR fitting function.

$a_0 = 36.59$	$a_1 = 0.04017$	$b_1 = 0.06998$	$a_2 = -0.08918$
$b_2 = 0.0732$	$a_3 = -0.06034$	$b_3 = 0.03041$	$a_4 = -0.1132$
$b_4 = 0.05443$	$a_5 = -0.03743$	$b_5 = -0.0002794$	$w = 0.4731$

The corresponding fitting curve is shown in Figure 8.

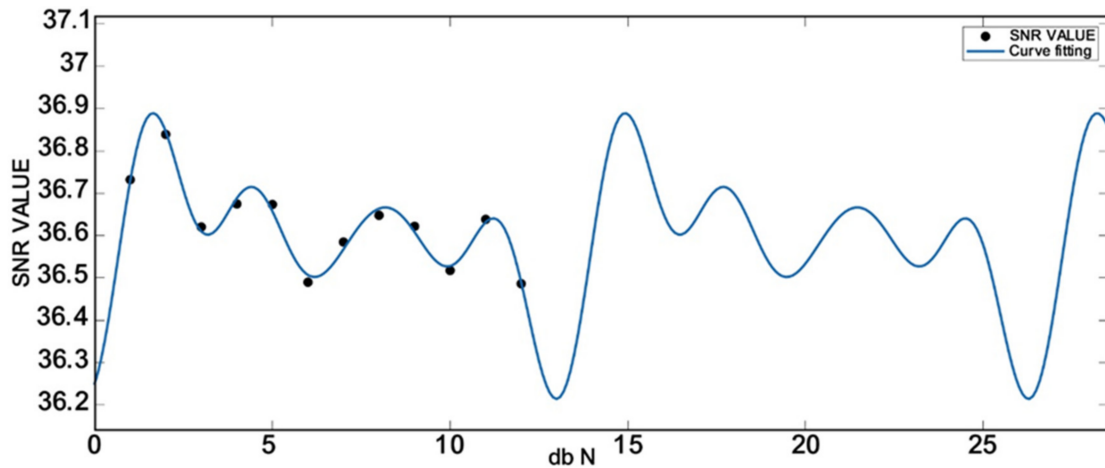


Figure 8. The SNR fitting curve of the db wavelet packet base.

The R^2 of this polynomial fit was 0.9844, and the fitting accuracy met the requirements of the maximum value of the SNR of the db wavelet packet base. The db wavelet packet base SNR value $f(b)_{max}$ was 36.8389.

Fourier curve fitting was performed on the MSE values corresponding to the wavelet packet bases of different orders of sym, and the Fourier fitting formula was obtained as follows.

$$f(x) = a_0 + a_1 \cos(xw) + b_1 \sin(xw) + a_2 \cos(2xw) + b_2 \sin(2xw) + a_3 \cos(3xw) + b_3 \sin(3xw) + a_4 \cos(4xw) + b_4 \sin(4xw) + a_5 \cos(5xw) + b_5 \sin(5xw) \tag{12}$$

The corresponding parameters of the fitting formula are shown in Table 5.

Table 5. The sym series wavelet packet base corresponded to the parameter value of the MSE fitting function.

$a_0 = 1.389$	$a_1 = -0.003555$	$b_1 = -0.02018$	$a_2 = 0.0003253$
$b_2 = -0.005518$	$a_3 = 0.02447$	$b_3 = -0.02445$	$a_4 = 0.01532$
$b_4 = 0.003341$	$a_5 = -0.01182$	$b_5 = 0.0009305$	$w = 0.5068$

The corresponding fitting curve is shown in Figure 9.

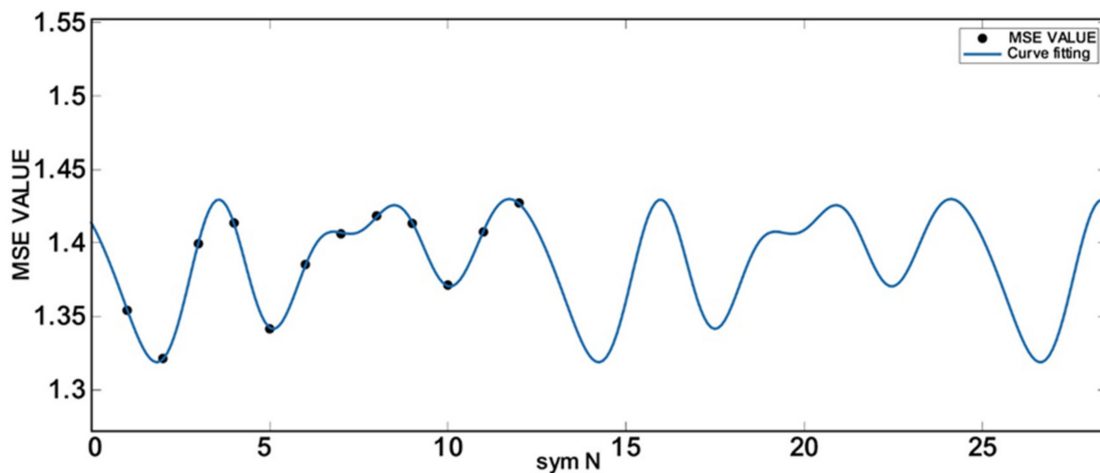


Figure 9. The sym wavelet packet base MSE fitting curve.

The R^2 of the polynomial fit was 0.9996, and the fitting accuracy met the extremely small value of the MSE of the sym wavelet packet base. The minor value of the MSE of the sym wavelet packet base $f(c)min$ was 1.3213.

Fourier curve fitting was performed on the SNR values corresponding to the wavelet packet bases of different orders of sym, and the Fourier fitting formula was obtained as follows.

The corresponding parameters of the fitting formula are shown in Table 6.

$$f(x) = a_0 + a_1 \cos(xw) + b_1 \sin(xw) + a_2 \cos(2xw) + b_2 \sin(2xw) + a_3 \cos(3xw) + b_3 \sin(3xw) + a_4 \cos(4xw) + b_4 \sin(4xw) + a_5 \cos(5xw) + b_5 \sin(5xw) \tag{13}$$

Table 6. The sym series wavelet packet base corresponded to the parameter values of the SNR fit function.

$a_0 = 36.62$	$a_1 = 0.01159$	$b_1 = 0.06443$	$a_2 = -0.0009322$
$b_2 = 0.0179$	$a_3 = -0.07799$	$b_3 = 0.07653$	$a_4 = -0.04938$
$b_4 = -0.01174$	$a_5 = 0.03721$	$b_5 = -0.002947$	$w = 0.5074$

The corresponding fitting curve is shown in Figure 10.

The R^2 of the polynomial fit was 0.9996, and the fitting accuracy met the requirements of the great value of the SNR of the sym wavelet packet base. The maximum value of the SNR of the sym wavelets $f(x)max$ was 36.8389.

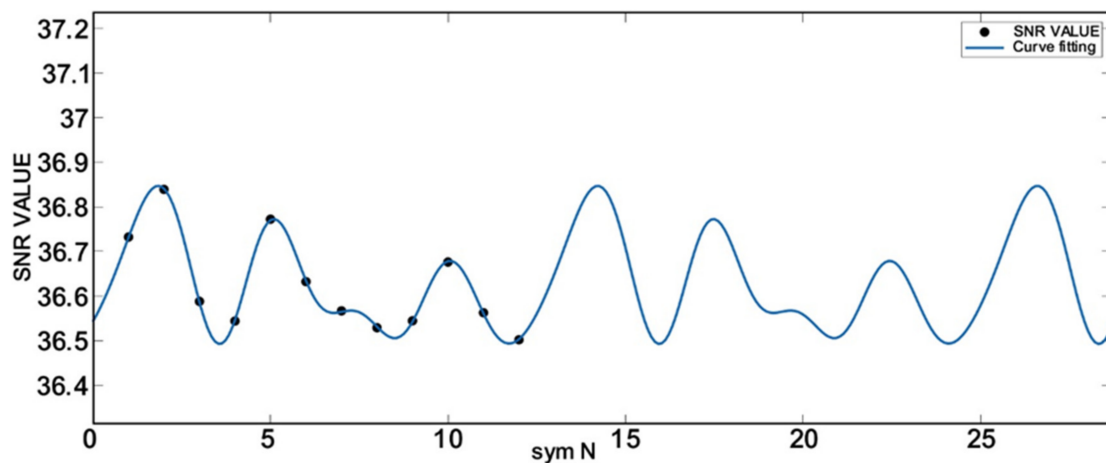


Figure 10. The SNR fit curve of the sym wavelet packet base.

The values of the MSE and SNR of Haar (haar), Dmeyer (dmey), BiorSplines (bior), ReverseBior (rbio), Coiflets (coif), and the Fejér–Korovkin (fk) finite order wavelet packet base are shown in Table 7.

Table 7. The MSE and SNR of the haar, dmey, bior, rbio, coif, fk wavelet packet base.

Wavelet Packet Base	MSE	SNR	Wavelet Packet Base	MSE	SNR
haar	1.3867	36.6291	rbio 1.3	1.4672	36.3840
dmey	1.4553	36.4168	rbio 1.5	1.6119	35.9748
bior 1.3	1.3166	36.8543	rbio 2.2	1.4232	36.5151
bior 1.5	1.4407	36.4621	rbio 2.4	1.3220	36.8363
bior 2.2	1.6239	35.9424	rbio 2.6	1.3933	36.6075
bior 2.4	1.3496	36.7465	rbio 2.8	1.3866	36.6285
bior 2.6	1.3824	36.6414	rbio 3.1	2.2907	34.4489
bior 2.8	1.3646	36.6978	rbio 3.3	1.4753	36.3598
bior 3.1	6.4503	29.9554	rbio 3.5	1.4547	36.4198
bior 3.3	1.9288	35.1958	rbio 3.7	1.3718	36.6752
bior 3.5	1.5646	36.1035	rbio 3.9	1.3718	36.6750
bior 3.7	1.4093	36.5579	fk 4	1.3307	36.8085
coif 1	1.4168	36.5348	fk 6	1.3724	36.6733
coif 2	1.3994	36.5879	fk 8	1.3713	36.6767
coif 3	1.4208	36.5218	fk 14	1.3773	36.6571
coif 4	1.4008	36.5836	fk 18	1.4258	36.5062
coif 5	1.4443	36.4499	fk 22	1.4485	36.4374

From Tables 2 and 7, fit Equations (9), (11)–(13), the signal can be decomposed by three layers, the maximum SNR removal noise was 36.8543, and the minimum MSE was 1.3166, corresponding to the small wavebase bior 1.3 wavelet packet base, so this article selected the bior 1.3 wavelet packet base to remove the signal of the PID.

3.3. Self-Adaptive Weight Threshold Denoise Method Based on a Wavelet Decomposition Node Energy

The wavelet decomposition was divided by the frequency band of the signal, and the sub-generation component of the low-frequency signal was obtained, so the characteristic information of the original signal also existed in the signal of each child. The characteristics of the signal can be analyzed through the energy of the wavelet decomposition node. After the signal is decomposed by a wavelet, the energy distribution characteristics in each frequency band can be used as an important basis for the signal distribution features.

The determination of the threshold and threshold function is the key to the problem of threshold. Traditional threshold-free noise is divided into two types: soft threshold function and hard threshold function. The wavelets are changed to adjust the wavelet

coefficient sequence $\theta + \gamma$. Among them, θ is the small wave packet coefficient of the signal, and γ is the wavelet coefficient of the wavelet.

Soft threshold: η is a threshold to destroy the son, that is, the threshold function; λ is the threshold.

$$\eta = \begin{cases} \text{sgn}(\theta + \gamma) (|\theta + \gamma| - \lambda), & |\theta + \gamma| \geq \lambda \\ 0, & |\theta + \gamma| < \lambda \end{cases} \quad (14)$$

Hard threshold:

$$\eta = \begin{cases} \theta + \gamma, & |\theta + \gamma| \geq \lambda \\ 0, & |\theta + \gamma| < \lambda \end{cases} \quad (15)$$

Since the low-frequency part of the signal's small waves contain most of the energy of the signal, as shown in the energy chart of the small wave decomposition node in Figure 5, we kept all of the low-frequency part of the signal. For the weight of the non-low-frequency part according to the weight of its signal energy, it will give corresponding weights to the corresponding weight, so the value retains its energy to remove the PID signal noise. The weight of each node's energy is as shown in Equation (14). Among them, $E_{i,j}$ can be calculated by Equation (2), S is the weight of the energy of the wavelet decomposition node.

$$S = \frac{E_{i,j}}{E_{\text{total}}} \quad (16)$$

Based on the threshold of the tide decomposition node energy self-adaptive weight, the noise removal method is:

$$\eta = \begin{cases} \text{sgn}(S\theta + \gamma) (|S\theta + \gamma| - \lambda), & |S\theta + \gamma| \geq \lambda \\ 0, & |S\theta + \gamma| < \lambda \end{cases} \quad (17)$$

According to the weight value of the wavelet coefficient, the preservation ratio of the energy of the non-low-frequency node is determined, so wavelet coefficient reconstruction was performed to remove the noise of the signal. After the signal noise removal, the SNR of the signal was 36.8543, and the MSE was 1.3166; the traditional wavelet package noise SNR was 33.8054, and the MSE was 2.6828, added indicators than the use of traditional wavelets, as shown in Figure 11.

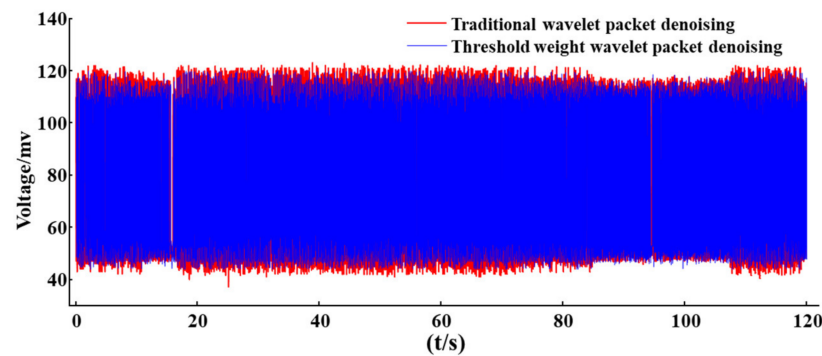


Figure 11. Comparison of the denoising effect between the traditional wavelet packet and threshold weight wavelet packet.

4. Conclusions

This study controlled the sensor through a single-chip microcomputer to achieve the sensor signal collected by the single-chip microcomputer and passed the sensor signal to the computer through the serial port. The optimal scale of wavelet decomposition was determined by the signal quality evaluation method, and the extreme values of MSE and SNR in the db and sym wavelet packet basis function with N-order wavelet packet base function were determined by the Fourier curve fitting method. The SNR and MSE values of the signal processed by the finite order wavelet base were calculated. The bior 1.3 wavelet

packet base was determined to be the optimal wavelet packet base for PID signal denoising. Aiming at the problem that the high frequency signal is not processed after wavelet packet decomposition, which leads to the loss of more details after signal denoising, the PID signal denoising method based on the adaptive weight of the node energy of the wavelet packet decomposition was proposed, and the signal quality after the traditional wavelet packet denoising and the signal processing method in this paper were compared. It was verified that the proposed method has the advantage of improving the high quality of the PID signal.

Author Contributions: Conceptualization, X.F.; methodology, X.F. and Z.L.; software, Z.L. and C.D.; validation, Z.L., C.D. and M.J.; formal analysis, Z.L.; investigation, Z.L., X.F., C.D. and M.J.; resources, X.F.; data curation, Z.L. and C.D.; writing—original draft preparation, Z.L.; writing—review and editing, X.F.; visualization, Z.L. and C.D.; supervision, Z.L., X.F., C.D. and M.J.; project administration, X.F.; funding acquisition, X.F. All authors have read and agreed to the published version of the manuscript.

Funding: This research was funded by [Shandong Province Key R&D Program] grant number [2021CXGC011206] And [The Graduate Innovation Program of China University of Mining and Technology] grant number [2022WLJCRCZL008] And [The Postgraduate Reserach&Practice Innovation Program of Jianguo Province] grant number [SJCX22_1144].

Institutional Review Board Statement: Exclude this statement.

Informed Consent Statement: Exclude this statement.

Data Availability Statement: Exclude this statement.

Conflicts of Interest: The authors declare no conflict of interest.

References

1. Kesselmeier, J.; Staudt, M. Biogenic volatile organic compounds (VOC): An overview on emission, physiology and ecology. *J. Atmos. Chem.* **1999**, *33*, 23–88. [[CrossRef](#)]
2. Kamal, M.S.; Razzak, S.A.; Hossain, M.M. Catalytic oxidation of volatile organic compounds (VOCs)—A review. *Atmos. Environ.* **2016**, *140*, 117–134. [[CrossRef](#)]
3. Zhang, Q.; Xia, B.; Yang, Z.; Chen, J. Research on the definition and characterization of volatile organic compounds. *Pollut. Control Technol.* **2014**, *27*, 3–7.
4. Zhang, X.; Xue, Z.; Sun, X.; Chai, H. Control status and countermeasures of atmospheric volatile organic compounds in China. *Environ. Sci. Manag.* **2014**, *39*, 16–19.
5. Wang, Q.; Zhou, G.; Zhong, Q.; Zhao, J.; Yang, K. Status and needs research for on-line monitoring of VOCs emissions from stationary sources. *Huan Jing Ke Xue = Huanjing Kexue* **2013**, *34*, 4764–4770.
6. Meng, F.; Zheng, H.; Chang, Y.; Zhao, Y.; Li, M.; Wang, C.; Sun, Y.; Liu, J. One-step synthesis of Au/SnO₂/RGO nanocomposites and their VOC sensing properties. *IEEE Trans. Nanotechnol.* **2018**, *172*, 212–219. [[CrossRef](#)]
7. Meng, F.; Li, X.; Yuan, Z.; Lei, Y.; Qi, T.; Li, J. Ppb-Level Xylene Gas Sensors based on Co₃O₄ Nanoparticles coated Reduced Graphene Oxide(rGO) Nanosheets Operating at Low Temperature. *IEEE Trans. Instrum. Meas.* **2021**, *70*, 9511510. [[CrossRef](#)]
8. Qin, W.; Yuan, Z.; Gao, H.; Zhang, R.; Meng, F. Perovskite-structured LaCoO₃ modified ZnO gas sensor and investigation on its gas sensing mechanism by first principle. *Sens. Actuators B Chem.* **2021**, *341*, 130015. [[CrossRef](#)]
9. Meng, F.; Shi, X.; Yuan, Z.; Ji, H.; Qin, W.; Shen, Y.; Xing, C. Detection of Four Alcohol Homologue Gases by ZnO Gas Sensor in Dynamic Interval Temperature Modulation Mode. *Sens. Actuators B Chem.* **2022**, *350*, 130867. [[CrossRef](#)]
10. Rezende, G.C. Microfabricated Modular Photoionization Detector for Volatile Organic Compounds. Doctoral Dissertation, University of Limerick, Limerick, Ireland, 2019.
11. Agbroko, S.O.; Covington, J. A novel, low-cost, portable PID sensor for the detection of volatile organic compounds. *Sens. Actuators B Chem.* **2018**, *275*, 10–15. [[CrossRef](#)]
12. Liu, C. Development of On-Line VOC Detector. Master's Thesis, Harbin Institute of Technology, Harbin, China, 2016.
13. Bilek, J.; Maršolek, P.; Bilek, O.; Buček, P. Field Test of Mini Photoionization Detector-Based Sensors—Monitoring of Volatile Organic Pollutants in Ambient Air. *Environments* **2022**, *9*, 49. [[CrossRef](#)]
14. Je, C.; Stone, R.; Oberg, S.G. Development and application of a multi-channel monitoring system for near real-time VOC measurement in a hazardous waste management facility. *Sci. Total Environ.* **2007**, *382*, 364–374. [[CrossRef](#)] [[PubMed](#)]
15. Mahmud, M.M.; Seok, C.; Wu, X.; Şennik, E.; Biliroğlu, A.Ö.; Adelegan, O.J.; Kim, I.; Jur, J.S.; Yamaner, F.Y.; Oralkan, Ö. A Low-Power Wearable E-Nose System Based on a Capacitive Micromachined Ultrasonic Transducer (CMUT) Array for Indoor VOC Monitoring. *IEEE Sens. J.* **2021**, *21*, 19684–19696. [[CrossRef](#)]

16. Hagens, L.A.; Verschuere, A.R.; Lammers, A.; Heijnen, N.F.; Smit, M.R.; Nijssen, T.M.; Geven, I.; Schultz, M.J.; Bergmans, D.C.; Schnabel, R.M.; et al. Development and validation of a point-of-care breath test for octane detection. *Analyst* **2021**, *146*, 4605–4614. [[CrossRef](#)] [[PubMed](#)]
17. Praveenchandar, J.; Vetrihangam, D.; Kaliappan, S.; Karthick, M.; Pegada, N.K.; Patil, P.P.; Rao, S.G.; Umar, S. IoT-Based Harmful Toxic Gases Monitoring and Fault Detection on the Sensor Dataset Using Deep Learning Techniques. *Sci. Program.* **2022**, *2022*, 7516328. [[CrossRef](#)]
18. Alyasseri, Z.A.A.; Khader, A.T.; Al-Betar, M.A.; Abasi, A.K.; Makhadmeh, S.N. EEG signals denoising using optimal wavelet transform hybridized with efficient metaheuristic methods. *IEEE Access* **2019**, *8*, 10584–10605. [[CrossRef](#)]
19. Zhang, Y.; Wang, R.; Li, S.; Qi, S. Temperature sensor denoising algorithm based on curve fitting and compound kalman filtering. *Sensors* **2020**, *20*, 1959. [[CrossRef](#)]
20. Hall, L.T.; Maple, J.L.; Agzarian, J.; Abbott, D. Sensor system for heart sound biomonitor. *Microelectron. J.* **2000**, *31*, 583–592. [[CrossRef](#)]
21. Rezende, G.C.; Le Calvé, S.; Brandner, J.J.; Newport, D. Micro photoionization detectors. *Sens. Actuators B Chem.* **2019**, *287*, 86–94. [[CrossRef](#)]
22. Langhorst, M.L. Photoionization detector sensitivity of organic compounds. *J. Chromatogr. Sci.* **1981**, *19*, 98–103. [[CrossRef](#)]
23. Ševčík, J.; Krýsl, S. A photoionization detector. *Chromatographia* **1973**, *6*, 375–380. [[CrossRef](#)]
24. Li, H. VOCs Detection Based on Photoionization Technology. Master's Thesis, Chongqing University of Posts and Telecommunications, Chongqing, China, 2019.
25. Zhou, Q.; Zhang, S.; Zhang, X.; Zhou, W.; Li, J.; Zhao, Y. Optimization of ionization chamber structure and experimental study of photoionization detector. *Chin. J. Transducer Technol.* **2018**, *31*, 323–328.
26. Liu, R.; Hu, H. Design of Photoionization sensor for VOC Gas Detection. *Instrum. Tech. Sens.* **2020**, 1–5.
27. Wang, J. Research on the Technology of VOC Gas Concentration Detection System Based on PID Principle. Master's Thesis, North University of China, Taiyuan, China, 2021.
28. Luo, G.; Liang, X.; Li, H.; Lu, C.; Pan, L.; Zhang, S. Intelligent Kitchen Based on STC89C52RC Micro Control Unit. In *Cyber Security Intelligence and Analytics, Proceedings of the 2020 International Conference on Cyber Security Intelligence and Analytics (CSIA 2020), Haikou, China, 28–29 February 2020*; Springer: Cham, Switzerland, 2020; pp. 348–353.
29. Cong, Y.; Ding, L. Design of Intelligent Express Robot Control System Based on 51 Single Chip Microcomputer. *J. Sens. Technol. Appl.* **2019**, *7*, 150–157.
30. Putri, S.F.; Rahayu, I.F.D. Perancangan Dan Implementasi Sistem Informasi Penjualan Dan Pembelian Pada Koperasi Syari'ah Muslim Mandiri Sejahtera (Kammis) Menggunakan Visual Studio 2015 Dan MySQL. *J. TEDC* **2020**, *14*, 183–194.
31. Cody, M.A. The wavelet packet transform: Extending the wavelet transform. *Dr. Dobb's J.* **1994**, *19*, 44–46.
32. Himeur, Y.; Alsalemi, A.; Bensaali, F.; Amira, A. Robust event-based non-intrusive appliance recognition using multi-scale wavelet packet tree and ensemble bagging tree. *Appl. Energy* **2020**, *267*, 114877. [[CrossRef](#)]
33. Altabay, W.A. The Damage Identification in Laminate Composite Plate under Fatigue Load Using Wavelet Packet Energy Curvature Difference Transform. *Compos. Part C Open Access* **2022**, *9*, 100304. [[CrossRef](#)]
34. Wang, K.; Su, G.; Liu, L.; Wang, S. Wavelet packet analysis for speaker-independent emotion recognition. *Neurocomputing* **2020**, *398*, 257–264. [[CrossRef](#)]
35. Hindi, A.; Dwairi, M.O.; Alqadi, Z. Analysis of Digital Signals using Wavelet Packet Tree. *Int. J. Comput. Sci. Mob. Comput.* **2020**, *9*, 96–103.
36. Huang, D.; Cui, S.; Li, X. Wavelet packet analysis of blasting vibration signal of mountain tunnel. *Soil Dyn. Earthq. Eng.* **2019**, *117*, 72–80. [[CrossRef](#)]
37. Ekici, S.; Yildirim, S.; Poyraz, M. Energy and entropy-based feature extraction for locating fault on transmission lines by using neural network and wavelet packet decomposition. *Expert Syst. Appl.* **2008**, *34*, 2937–2944. [[CrossRef](#)]
38. Sun, Y.; Cao, Y.; Li, P. Fault diagnosis for train plug door using weighted fractional wavelet packet decomposition energy entropy. *Accid. Anal. Prev.* **2022**, *166*, 106549. [[CrossRef](#)]
39. Ling, T.H.; Li, X.B.; Dai, T.G.; Peng, Z.B. Features of energy distribution for blast vibration signals based on wavelet packet decomposition. *J. Cent. South Univ. Technol.* **2005**, *12*, 135–140. [[CrossRef](#)]

Disclaimer/Publisher's Note: The statements, opinions and data contained in all publications are solely those of the individual author(s) and contributor(s) and not of MDPI and/or the editor(s). MDPI and/or the editor(s) disclaim responsibility for any injury to people or property resulting from any ideas, methods, instructions or products referred to in the content.